2013

Vibrational Photoacoustic Tomography: Deep Tissue Imaging with Biomarker Sensitivity

Rui Li
Purdue University, lrrhwfy@hotmail.com

Graduate School ETD Form 9
(Revised 12/07)

PURDUE UNIVERSITY
GRADUATE SCHOOL
Thesis/Dissertation Acceptance

This is to certify that the thesis/dissertation prepared

By Rui Li

Entitled
Vibrational Photoacoustic Tomography: Deep Tissue Imaging with Biomarker Sensitivity

For the degree of Master of Science in Biomedical Engineering

Is approved by the final examining committee:

Prof. Ji-Xin Cheng
Chair

Prof. Michael Sturek

Prof. Young Kim

To the best of my knowledge and as understood by the student in the *Research Integrity and Copyright Disclaimer (Graduate School Form 20)*, this thesis/dissertation adheres to the provisions of Purdue University's "Policy on Integrity in Research" and the use of copyrighted material.

Approved by Major Professor(s): Prof. Ji-Xin Cheng

Approved by: George R. Wodicka 11/15/2013
Head of the Graduate Program Date

VIBRATIONAL PHOTOACOUSTIC TOMOGRAPHY: DEEP TISSUE IMAGING WITH BIOMARKER SENSITIVITY

A Thesis

Submitted to the Faculty

of

Purdue University

by

Rui Li

In Partial Fulfillment of the

Requirements for the Degree

of

Master of Science in Biomedical Engineering

December 2013

Purdue University

West Lafayette, Indiana

To my family and all my friends.

ACKNOWLEDGEMENTS

I would like to express my sincere gratitude to my advisor, Dr. Ji-Xin Cheng, and Cheng group for their support and encouragement through all my years in the United States. Special thanks to Pu Wang for all of his help with experimental design, for detailed discussions, and for mentoring. Thanks to Dr. Mikhail Slipchenko for your invaluable assistance with building the first Raman laser in our lab. I would also like to thank Dr. Justin Rajesh Rajian for his help with the setup of single element photoacoustic tomography imaging platform. Thanks to Dr. Michael Sturek and his lab for providing animal tissues precious thoughts for our experiment. Finally, thanks to my family and friends for all of your love and support.

TABLE OF CONTENTS

Page

Page

LIST OF FIGURES

Figure Page

LIST OF ABBREVIATIONS

Photoacoustic (PA)

Second harmonic generation (SHG)

Photoacoustic microscopy (PAM)

Photoacoustic tomography (PAT)

Photoacoustic endoscopy (PAE)

Two dimensional (2D)

Three dimensional (3D)

Hematoxylin-and-eosin (HE)

Optical parametric oscillator (OPO)

Stimulated Raman scattering (SRS)

Polarizing beam splitter (PBS)

Half-wave plate (HWP)

Quarter-wave plate (QWP)

Vibrational photoacoustic tomography (VPAT)

Data acquisition (DAQ)

Abdominal aortic aneurysm (AAA)

Angiotensin II (AngII)

Apolipoprotein $E^{-/-}$ ($apoE^{-/-}$)

ABSTRACT

Li, Rui. M.S.B.M.E., Purdue University, December 2013. Vibrational Photoacoustic Tomography: An Effective Method for Deep Tissue Imaging. Major Professor: Ji-Xin Cheng.

As a molecular and functional imaging modality, photoacoustic imaging has been applied to animals or human organs such as breast, brain and skin. Till now, the contrast mechanism of photoacoustic imaging is mainly based on electronic absorption in visible and near infrared region. Inherent molecular vibration offers a contrast mechanism for chemical imaging in a label free manner. In vibrational microscopy based on either infrared absorption or Raman scattering, the imaging depth is limited to the ballistic photon mean free path, which is a few hundred microns in a biological sample. Owing to much weaker acoustic scattering in tissues as compared to optical scattering, photoacoustic detection of harmonic molecular vibration has enabled significant improvement in imaging depth. Broad use of this modality is, however, hampered by the extremely low conversion efficiency of optical parametric oscillators at the overtone transition wavelengths. My thesis work aimed to overcome such barrier through construction of a high-energy Raman laser and proof-of-concept demonstration of vibrational photoacoustic tomography.

Our Raman laser is based on the process of stimulated Raman scattering in a gain medium. The output wavelength of a Raman laser was determined by the pump wavelength and Raman shifts of the medium. Using a 5-ns Nd:YAG laser as the pumping source, up to 21.4 mJ pulse energy at 1197 nm was generated, corresponding to a conversion efficiency of 34.8%. Using the 1197 nm pulses, three-dimensional photoacoustic imaging of intramuscular fat was demonstrated (J Biomed Optics 2013).

Further, by using a larger $Ba(NO_3)_2$ crystal and no prior focusing of input laser, I recently constructed a new Raman laser, which could produce stable laser pulses at 1197 nm with maximum pulse energy exceeding 100 mJ. Using the new Raman laser, we demonstrated proof-of-concept of vibrational photoacoustic tomography with C-H rich polyethylene tube phantom placed under 3 cm thick chicken breast tissue (J Phys Chem Lett 2013). Furthermore, by modification of a commercial ultrasound machine, photoacoustic/ultrasound dual-modality real-time *in vivo* imaging of biological tissues is fulfilled (unpublished). These developments open exciting opportunities of performing label free vibrational imaging in the deep tissue regime.

CHAPTER 1. INTRODUCTION

1.1 Photoacoustic Effect

The photoacoustic (PA) effect, also known as optoacoustic effect, refers to the formation of acoustic waves followed by the absorption of light energy, which could be in the format of modulated light or pulsed light. In 1880, Alexander Graham Bell first observed the sound generation from a solid sample exposed to the modulated sun light. [1-2] Since then, the photoacoustic effect has been used to measure the light absorption spectrum,[3] estimate the chemical energies stored in a photochemical reaction[4] and so on.

1.2 Photoacoustic Imaging in Biomedicine

In pure optical imaging modalities, imaging depth is limited to millimeter level by optical scattering in soft tissues, such as confocal microscopy, second harmonic generation (SHG), and coherent Raman imaging. [5-7] Meanwhile, ultrasound scattering in biological samples is two to three orders of magnitude smaller than optical scattering, which could lead to a better resolution in deep tissues.[8] However, pure ultrasound imaging is based on detecting mechanical properties of biological tissues, which could not provide chemical information of the imaging target. The emergence of photoacoustic imaging overcomes the aforementioned problem with high resolution images in deep tissue regime.

Phtotoacoustic imaging is directly developed on the basis of photoacoustic effect, which could be considered as an ultrasound imaging modality with light absorption contrast. Upon the absorption of non-ionizing ns laser pulses on the biological tissues, some of the absorbed energy will be converted into heat, resulting in a tiny local

temperature rise, usually in the millikelvin range. Then, the following transient thermoelastic expansion will usually travel in the form of ultrasonic waves with MHz central frequency, which could be detected by the ultrasonic receivers placed around the samples. Based on time of flight, the spatial information of the sample encoded in the ultrasound could be reconstructed. The amplitude of photoacoustic signal is proportional to the volume expansion coefficient and the speed of ultrasound, which are both temperature dependent for water-based tissues.

1.2.1 Optical Properties of Biological Tissues

There are three general parameters that describe the interaction of photons with biological tissues: absorption of light, scattering of light, and fluorescence emission. Optical absorption properties can be applied to quantify hypermetabolism and angiogenesis,[9-10] while optical scattering properties can uncover architectural characteristics of biological samples.[11] Optical absorption in biological tissues is dependent on the chemical composition. The light absorption by endogenous chromospheres in living tissues (including hemoglobin and melanin[12-13]) is typically within the visible spectral region (400 – 700 nm), limiting light penetration to only a few millimeters. Meanwhile, above 900 nm, light absorption due to water is increasingly higher.[14] Light scattering in tissues could be described by the reduced scattering coefficient, $\mu_s^{'} = \mu_s(1-g)$, where μ_s is the scattering coefficient and g is the anisotropy factor. Generally, in the visible and near infrared region, μ_s is 100 cm^{-1} and g is 0.9, while the absorption coefficient μ_a is varied between 0.1 and 10 cm^{-1} in tissues.[15] In deep tissues, multiple scattering results in the loss of directionality. Therefore, resolution of pure optical imaging dependent on the ballistic photons will be compromised. Accordingly, the imaging depth will be restricted to one photon transport mean free path (~ 1 mm). Nevertheless, PA imaging is based on the detection of light absorption. Not only ballistic photons, but also diffused photons could contribute to the

photoacoustic signal generation. Therefore, deeper imaging regime could be reached with higher resolution resulted from less ultrasound scattering in biological tissues.

1.2.2 Traditional Photoacoustic Imaging

With optical absorption contrast and ultrasonic spatial resolution, photoacoustic imaging has been applied to animals or human organs such as breast, brain and skin.[16-20] In PA imaging, pulsed light is used to induce optical absorption inside a tissue by diffused photons. Part of the absorbed energy is converted into heat, which raises the temperature of the absorbed region on the order of mK. The temperature rise is proportional to a tissue-dependent constant, which could be experimentally determined. This sudden temperature change then creates pressure transients and subsequent generation of photoacoustic waves detectable by an ultrasonic transducer in real time. From the measured signal, the distribution of optical absorbers is reconstructed. Till now, the contrast mechanism of photoacoustic imaging is mainly based on electronic absorption in visible and near infrared region extending up to 950 nm. Photoacoustic imaging of hemoglobin[21-23] and exogenous contrast agents such as dyes and nanoparticles[24-27] has been reported. Currently, photoacoustic imaging mainly has three implementations: photoacoustic microscopy (PAM), photoacoustic tomography (PAT), and photoacoustic endoscopy (PAE). Usually, PAM and PAE can be used to fulfill millimeter depth with micrometer resolution, while PAT could reach centimeter imaging depth.

1.2.2.1 Photoacoustic Microscopy

In PAM, both optical excitation and acoustic detection are focused, and the dual foci are configured confocally to optimize the imaging performance. In the configuration, a two dimensional (2D) scanning stage is usually employed to achieve 3D imaging. The lateral resolution is determined by the overlap of the dual foci, while the axial resolution is determined by the acoustic time of flight. The imaging depth is mainly limited by the

ultrasonic attenuation. The typical configuration of PAM is shown in **Figure 1-1 (a)**.[28] The laser pulse is focused by an objective for the excitation in the tissue. An optical-acoustic beam combiner, composed of two prisms bonding with silicone oil, is located underneath the objective. An achromatic correction lens is attached on the top of the prism to offset the optical aberration. The ultrasound transducer is placed on the surface of another prism to collect generated photoacoustic signals. Based on similar experimental setup, multi-wavelength PAM has been used for in vivo label-free functional imaging of hemoglobin oxygen saturation in vessels[29] (**Figure 1-2**) and *in vivo* imaging of a subcutaneously inoculated melanoma in an immunocompromised nude mouse. [20] (**Figure 1-3**)

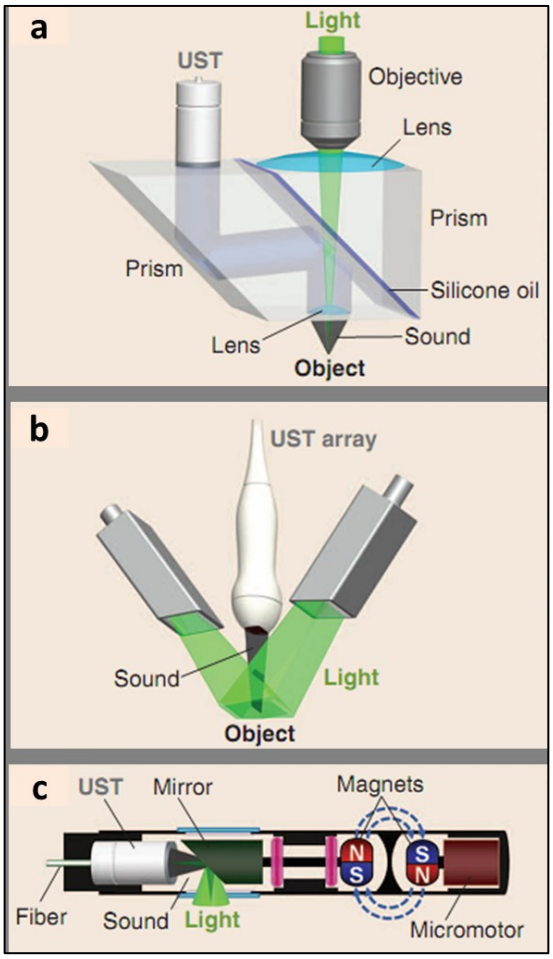

Figure 1-1: Major embodiments of PA imaging.[28] (a) Photoacoustic microscopy. (b) Photoacoustic tomography. (c) Photoacoustic endoscopy.

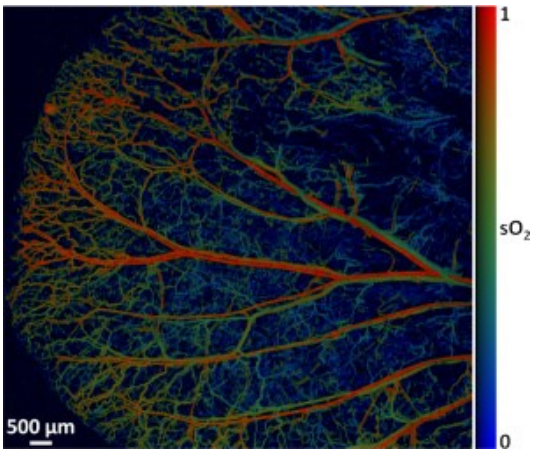

Figure 1-2: Dual-wavelength (561 nm and 570 nm) optical resolution photoacoustic microscopy of hemoglobin oxygen saturation in a living mouse ear.[29]

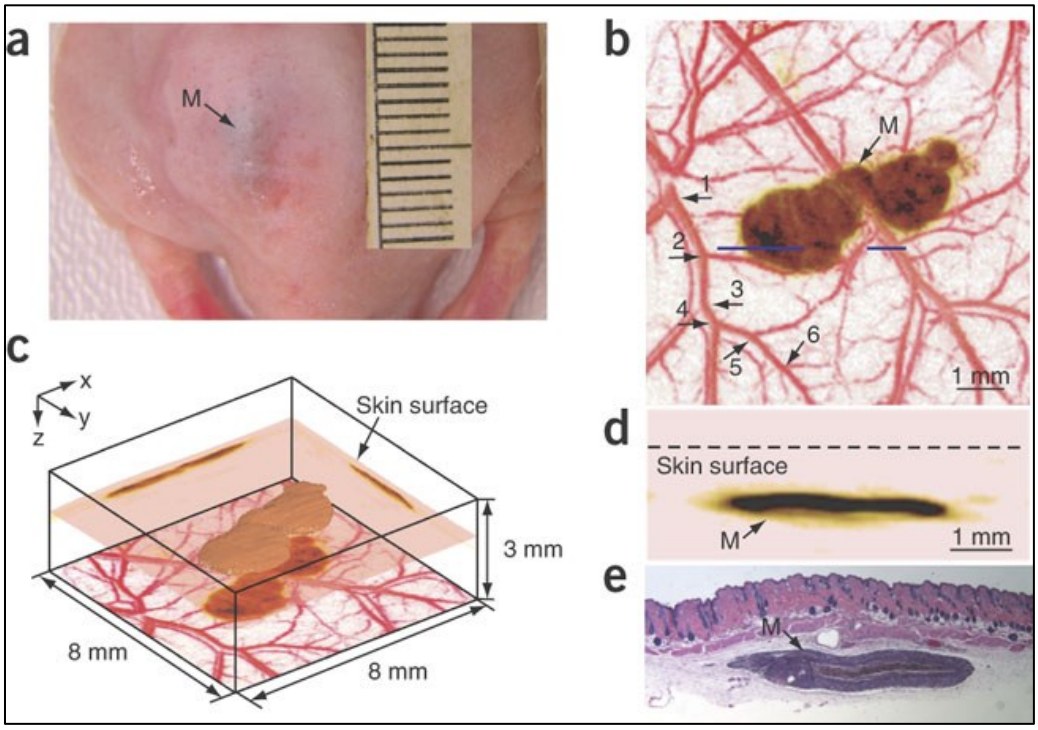

Figure 1-3: *In vivo* photoacoustic imaging of a subcutaneously inoculated melanoma in an immunocompromised nude mouse.[20] (a) Photograph of the melanoma. (b) A composite of the two maximum-amplitude projection images. (c) Three-dimensional rendering of the melanoma from the data acquired at 764 nm. (d) An enlarged cross-sectional image of the melanoma. (e) Hematoxylin-and-eosin (HE) stained section at the same marked location.

1.2.2.2 Photoacoustic Tomography

In PAT, unfocused laser light is used for excitation, along with unfocused ultrasound transducer for PA signal detection. The imaging depth is not limited by the ultrasound transducer but is mainly determined by the extent of light penetration. Since unfocused light is employed, higher laser energies could be applied to illuminate the sample, which will lead to deeper light penetration. In linear-array PAT (**Figure 1-1 (b)**)[28], a multimode fiber bundle is integrated with the ultrasound transducer array for optical illumination. Based on a clinical ultrasound imaging system, this methodology could be adapted inherently for dual-modality imaging. Until now, PAT has been greatly used to image rat brain lesion *in situ* [18] (**Figure 1-4**) and hemodynamics monitoring.[19] (**Figure 1-5**)

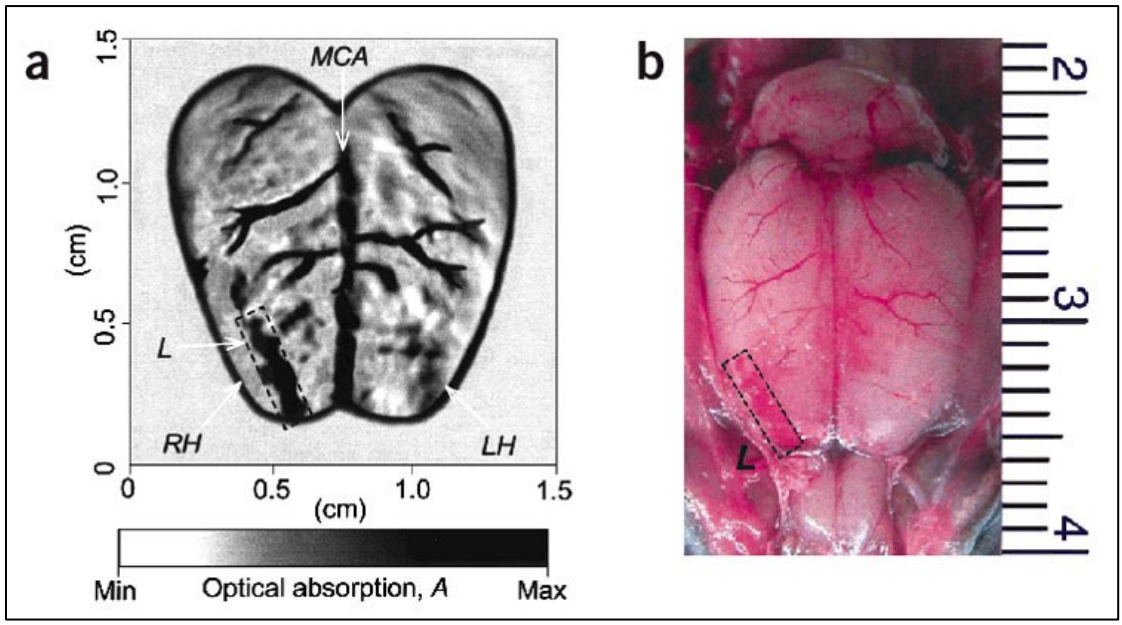

Figure 1-4: PAT imaging of the rat brain lesion in situ.[18] (a) Noninvasive PAT image of a superficial lesion on a rat's cerebra acquired with the skin and skull intact. (b) Open-skull photograph of the rat cerebral surface acquired after PAT imaging.

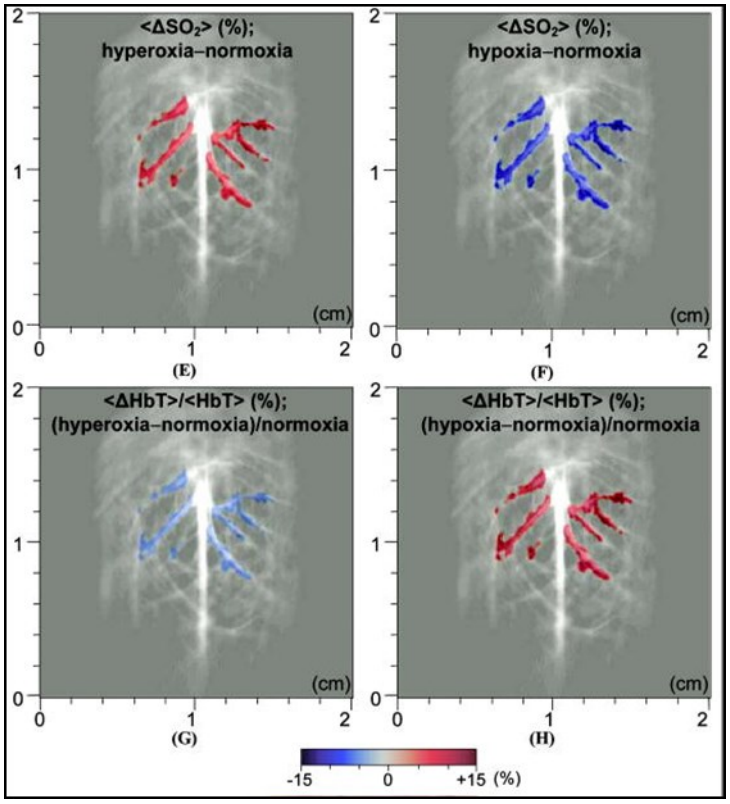

Figure 1-5: Noninvasive spectroscopic PAT imaging of the total concentration of hemoglobin and the hemoglobin oxygen saturation of a rat brain.[19]

1.2.2.3 Photoacoustic Endoscopy

In a representative design (**Figure 1-1 (c)**)[28], laser light is delivered by a multimode fiber placed in the center hole of a ring ultrasound transducer. Driven by a micromotor, an optically and acoustically coupled mirror could rotate for circular scanning. What's more, a linear motor is used for pulling back the probe, in order to fulfill 3D PA imaging. Generally, PAE is specially designed, which can be used for imaging internal organs, such as esophagus, colon and vessels.[30-33]

CHAPTER 2. VIBRATIONAL PHOTOACOUSTIC IMAGING WITH A RAMAN LASER

2.1 Introduction

As a molecular and functional imaging modality, photoacoustic tomography has proved the imaging capability of several centimeters deep into biological samples.[34-37] Until now, the majority of the PA imaging studies has been based on electronic absorption of molecules and nanostructures. Photoacoustic imaging employing molecular overtone vibration as a contrast mechanism opens a new avenue for bond-selective imaging of deep tissues. In particular, overtones of C-H bond vibration have been adopted to visualize lipid and collagen.[30, 38-42] In order to resonate with C-H bond vibration, laser wavelengths at 1210 nm or 1730 nm are used, where the absorption peaks of the second and first overtone reside.[43] Currently, the optical parametric oscillator (OPO) pumped by harmonics of Nd:YAG laser is employed to generate the necessary wavelengths.[30, 38-41] However, the conversion efficiency at the aforementioned specific wavelengths is very low, making it difficult to generate high pulse energy needed for vibrational PA tomography. In addition, the cost of an OPO often exceeds that of the pump laser. Therefore, there is a crucial need of a laser system with high pulse energy for photoacoustic imaging with CH- bond vibration as the contrast.

2.2 Solid-state Raman Laser

2.2.1 Introduction

The Raman laser, also called Raman shifter, is based on the process of stimulated Raman scattering (SRS) in a gain medium. The output wavelength of a Raman laser is

determined by the pump wavelength and Raman shifts of the medium. SRS is a nonlinear optical conversion process, which could shift the wavelength of a laser light to another wavelength. It could occur in gases, liquid, and crystals. Therefore, Raman laser could operate on the basis of media with different forms.

Gases have long been used as the Raman media, mainly due to its low scattering losses. The most common gases are H_2, D_2, and CH_4.[44-46] However, the large physical size and low gain properties limit its applications. Although liquid is also used as the Raman gain medium, its toxicity of the materials inherently hinders its achievement.[47-49] By virtue of their high gain and good thermal and mechanical properties, crystalline materials have successfully and greatly used to extend spectral coverage of solid-state lasers.[50-55] The most promising and commercialized Raman crystals reported in the literature are $LiIO_3$, $Ba(NO_3)_2$, $KGd(WO_4)_2$, and $CaWO_4$. Their properties are shown in **Figure 2-1**. [56]

Material	Frequency shift (cm^{-1})	Raman line width $\Delta\Omega_R$ (cm^{-1})	Integral cross section Σ_{int} (a.u.)	Peak intensity Σ_{peak} (a.u.)	Excitation geometry	
					K	E
Diamond	1333	2.7	100	100	$//C_3$	$\perp C_3$
$CaWO_4$	911	4.8	52	18	$\perp C_4$	$//C_4$
$SrWO_4$	921	2.7	50	41	$\perp C_4$	$//C_4$
$BaWO_4$	925	1.6	52	64	$\perp C_4$	$//C_4$
$KGd(WO_4)_2$	901	5.4	50	35	$\perp C_2$	$\perp C_2$
$KGd(WO_4)_2$	767	5.4	59	37	$\perp C_2$	$//C_2$
$Ba(NO_3)_2$	1048	0.4	21	63	$//C_4$	$//C_4$
$NaNO_3$	1069	1	23	44	$//C_3$	$\perp C_3$
$CaCO_3$	1086	1.2	6	10.6	$//C_3$	$\perp C_3$
$LiIO_3$	821	5	54	25	$//C_2$	$\perp C_2$

Figure 2-1: Spontaneous Raman scattering parameters of crystals.[56]

The $Ba(NO_3)_2$ crystal is an isotropic material with cubic symmetry. At room temperature, the Raman gain coefficient of $Ba(NO_3)_2$ crystal is 11 cm/GW, pumped by 1064 nm Nd:YAG laser. The optical damage threshold is ca. 400 MW/cm^2. Its Raman spectrum is dominated by a strong peak at 1047 cm^{-1} (**Figure 2-2**)[57], which corresponds

to the "breathing" mode of the NO_3 molecular group.[51, 58] Therefore, if the $Ba(NO_3)_2$ crystal is pumped by 1064 nm Nd:YAG laser, 1197 nm laser will be generated based on SRS process. Since this wavelength falls in the second overtone absorption peak of CH-bond vibration, it will provide us great potentials to perform photoacoustic tomography imaging in deep tissue.

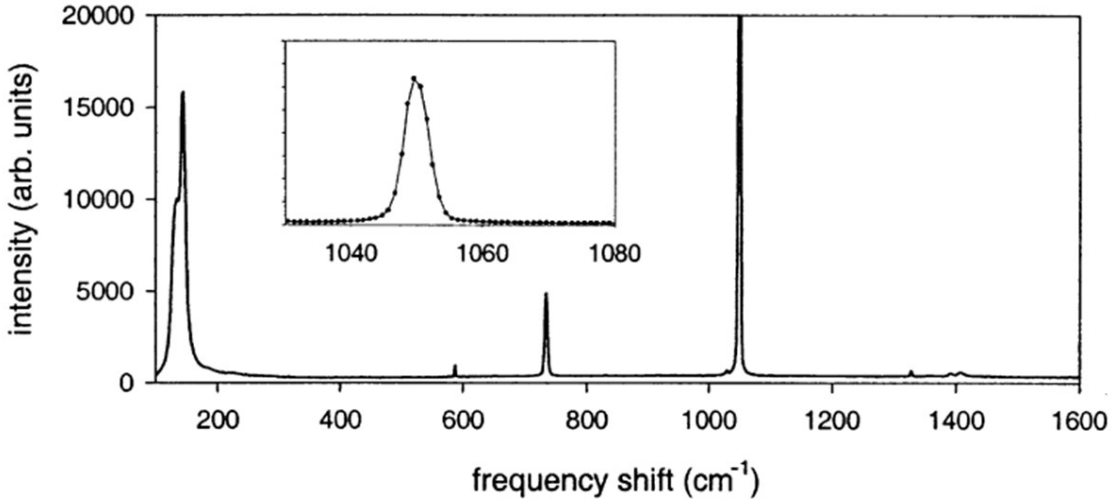

Figure 2-2: Spontaneous Raman spectra of $Ba(NO_3)_2$ crystal.[57]

2.2.2 Experimental Setup

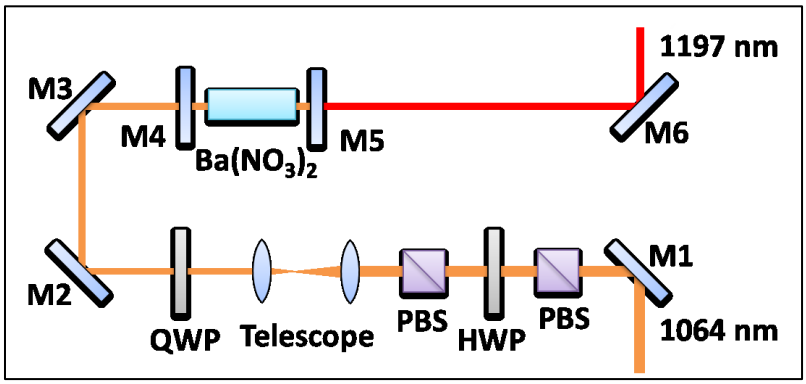

Figure 2-3: Schematic of the Raman laser based on $Ba(NO_3)_2$ crystal. M1, M2, and M3: 45° 1064 nm reflective mirror. PBS: polarizing beam splitter. HWP: half wave plate. QWP: quarter wave plate. M4: resonator end mirror. M5: output coupler. M6: silver mirror.

A schematic of our setup is shown in **Figure 2-3**. The $Ba(NO_3)_2$ crystal was pumped by a Q-switched Nd:YAG laser (Continuum Surelite SL III-10) operated with a 10 Hz repetition rate and 5 ns pulse duration (FWHM). A polarizing beam splitter (PBS) was used to purify the polarization of the fundamental 1064 nm laser light. A half-wave plate (HWP) and a second PBS were combined and used as a variable attenuator to adjust the pump pulse energy. A telescope composed of two positive lenses was employed to reduce the pump beam size to match the dimensions of the $Ba(NO_3)_2$ crystal. For the Raman laser, a flat-flat resonator with a cavity length of about 10 cm was used. The resonator end mirror (M4) was coated with high reflectivity at 1197 nm (R> 99%). The output coupler (M5) was coated with high reflectivity at 1064 nm (R>99%) and 40% transmission at 1197 nm. The $Ba(NO_3)_2$ crystal, with dimensions of 4×4×38 mm^3, was coated with high transmission at 1064 nm and 1197 nm on both faces.

2.2.3 Characteristics of the Raman Laser

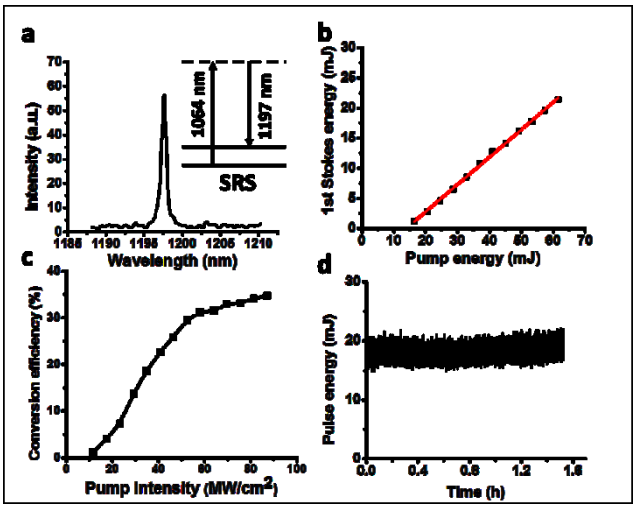

Figure 2-4: Characteristics of the $Ba(NO_3)_2$ crystal-based Raman laser. (a) Spectral profile of the Raman laser output. (b) The 1st Stokes energy as a function of the pump energy incident on the Raman crystal. Red solid line is a linear fit. (c) Conversion efficiency with respect to the pump intensity incident on the Raman crystal. (d) Pulse energy of Raman laser as a function of time.

Performances of the Raman laser are shown in **Figure 2-4**. The spectral profile of the Raman laser output, measured by the USB 2000 spectrometer (Ocean Optics), indicates the central wavelength of ca. 1197.6 nm (**Figure 2-4 (a)**). The maximum pump energy was limited to 60 mJ by crystal damage threshold, with maximum output pulse energy measured to be 21.4 mJ, corresponding to a slope efficiency of 45.4% (**Figure 2-4 (b)**). The key parameter, conversion efficiency, was defined as the pulse energy of the Raman laser divided by the pulse energy of the pump laser incident on the $Ba(NO_3)_2$ crystal. As shown in **Figure 2-4 (c)**, the maximum conversion efficiency is about 34.8%, which is much larger than 0.5%, the efficiency for the OPO system we used before (Panther EX Plus, Continuum). The threshold for the 1st Stokes Raman laser was measured to be 11.6 MW/cm^2. The discrepancy between the experimental value and the theoretical value (6.1 MW/cm^2) may arise from the optical losses resulted from deflection and diffraction. Variation of the 1st Stokes output energy obtained with 60 mJ pump energy (incident on the crystal) were plotted up to 1.5 hours, as shown in **Figure 2-4 (d)**. The maximum pulse energy drop was 12%, which may be caused by the fluctuation of the pump Nd:YAG laser (6%) and instability of the cavity.

2.3 Vibrational Photoacoustic Microscopy Based on a Raman Laser

2.3.1 Experimental Setup

Although 1197 nm locates in the second overtone absorption range of CH-bond, it is not the peak absorption wavelength. Therefore, it is necessary to check its photoacoustic imaging capability of CH-bond rich samples. Herein we demonstrate for the first time the use of aforementioned $Ba(NO_3)_2$ crystal-based Raman laser for vibration-based PA microscopic imaging. The imaging setup is shown in **Figure 2-5**. The 1197 nm Raman laser was directed into an inverted microscope (IX71, Olympus) for PA imaging. An achromatic doublet lens (30 mm focal length, Thorlabs) was applied to focus the Raman laser on the samples. The PA signals were detected by a focused ultrasonic transducer (V317, Olympus NDT), followed by a preamplifier (5682, Olympus NDT) and a pulse receiver (5073 PR-15-U, Olympus NDT). The collected PA signals were

then sent to a digitizer (USB-5133, National Instrument), and retrieved via a customized LabVIEW program. To perform 3D vibrational PA imaging, an XY translational stage (ProScan H117, Prior) was employed for raster scanning of samples.

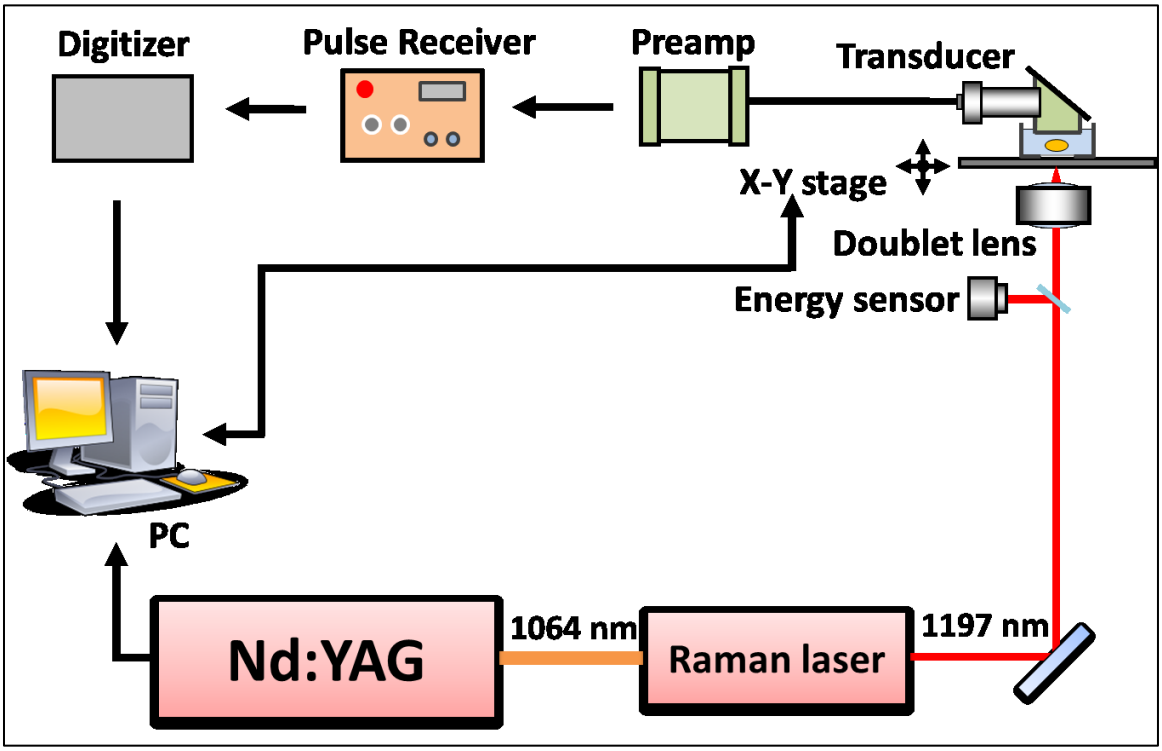

Figure 2-5: Schematic of a photoacoustic microscope equipped with a $Ba(NO_3)_2$ crystal-based Raman laser. PC: Computer.

2.3.2 Result and Discussion

Intramuscular fat was employed to demonstrate the capability of the Raman Laser for PA imaging. The muscle samples, which were cut into ~ 10×10×4 mm^3 pieces, were harvested from a goat and then preserved in fixative 10% buffered formalin. The small muscle piece was then placed in a glass bottom dish and embedded with H_2O-agarose gel for the subsequent PA imaging. With the pulse energy of 60 μJ on the sample, PA imaging of intramuscular fat was conducted, as shown in **Figure 2-6**. On-resonant and off-resonant PA images are shown in **Figure 2-6 (a-b)**. A strong signal was found at 1197 nm and the contrast nearly disappeared at 1064 nm. These data

demonstrate that PA signal is generated from the C-H bond overtone vibration of lipid. This lipid imaging capability was further confirmed by histological examination of the same tissue (**Figure 2-6 (c)**), where the same morphology of fat (white color) was observed. On the same setup, we further demonstrated 3D PA imaging of intramuscular fat (**Figure 2-6 (d)**), with an axial resolution of 110 µm, a lateral resolution of 60 µm and an imaging depth of ~ 3 mm.

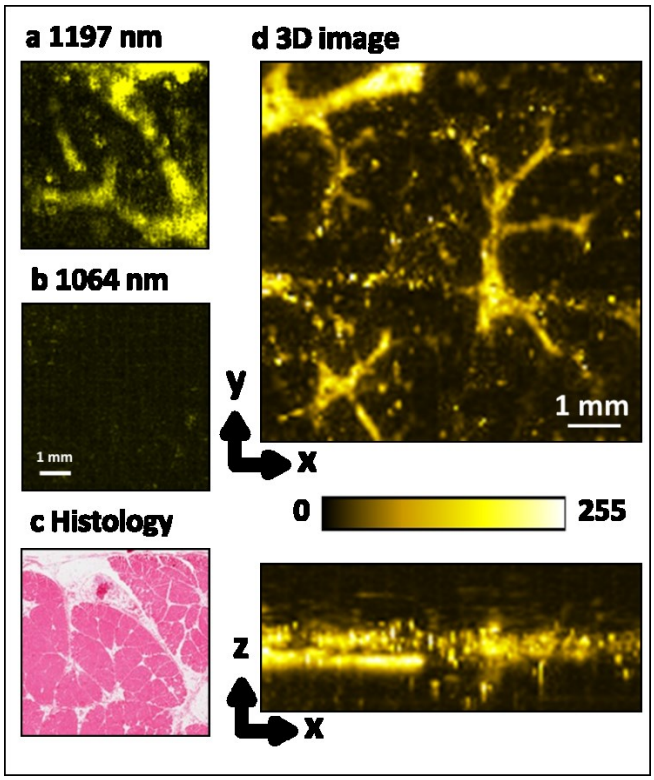

Figure 2-6: PA imaging of intramuscular fat performed with the Raman laser. (a) *En face* maximum intensity projection PA image of intramuscular fat sample with 1197 nm excitation. (b) *En face* maximum intensity projection PA image of intramuscular fat sample with 1064 nm excitation. (c) Histological evaluation of the same intramuscular fat sample. (d) Three-dimensional PA image of a separate intramuscular fat sample. Pulse energy: 60 µJ. Image size: 120×120 pixels.

2.3.3 Conclusion

In conclusion, we demonstrated PA imaging of lipids with a compact $Ba(NO_3)_2$ crystal-based Raman laser. Up to 21.4 mJ pulse energy at 1197 nm was produced,

corresponding to the conversion efficiency of 34.8%. The high conversion efficiency of the Raman laser would enable vibrational PA tomography by using a larger $Ba(NO_3)_2$ crystal to endure larger incident pulse energy and generate 100 mJ pulse energy at 1197 nm (currently under progress). Notably such energy is considered to be safe for human studies according to the American National Standard (Z136.1 – 2000). PA tomography with overtone vibration as contrast is expected to open new opportunities for bond-selective imaging of biological tissues with an imaging depth and field of view both on the centimeter scale.

2.4 Vibrational Photoacoustic Tomography with a Single Element Transducer

2.4.1 Principles

As a molecular and functional imaging modality, photoacoustic tomography has proved the imaging capability of several centimeters deep into biological tissues. In PAT, pulsed light is used to induce optical absorption inside a tissue by diffused photons. Part of the absorbed energy is converted into heat, which raises the temperature of the absorbed region on the order of mK. This sudden temperature change then creates pressure transients and subsequent generation of photoacoustic waves detectable by an ultrasonic transducer in real time. From the measured signal, the distribution of optical absorbers is reconstructed. Till now the contrast mechanism in PAT is mainly based on electronic absorption in near infrared region extending up to 950 nm. PAT imaging of hemoglobin[21-23] and exogenous contrast agents such as dyes and nanoparticles[24-27] has been reported. Inherent molecular vibration offers a contrast mechanism for chemical imaging in a label free manner. In vibrational microscopy based on either infrared absorption or Raman scattering, the imaging depth is limited to the ballistic photon mean free path, which is a few hundred microns in a biological sample. Owing to much weaker acoustic scattering in tissues as compared to optical scattering, photoacoustic detection of harmonic molecular vibration has enabled significant

improvement in imaging depth.[30, 38-39] In this method, optical absorption is induced by overtone transitions at near infrared wavelengths, such as the second overtone transition of C-H bond occurring around 1200 nm.[59] Upon excitation, this vibrational energy quickly turns into heat, which leads to bond-selective photoacoustic signals. Overtone transitions have been used for intravascular photoacoustic imaging of lipid accumulation.[30, 41] In these studies, focused high-frequency ultrasonic transducers were used. The transducer was moved along a line or rotated about its own axis, and the PA signals were required from the focused region. The image was then built by converting time into distance according to the speed of sound and signal amplitude into a color map. The image depth with a focused transducer was limited to its focused region, generally on the millimeter scale. Further, the imaging configuration, which is similar to PA microscopy, was limited to thin samples. Therefore, less energy per pulse illumination was required, which was possible through the use of existing laser sources.

Despite these advances, vibrational photoacoustic tomography, abbreviated as VPAT hereafter, is not yet demonstrated. Tomography uses an unfocused transducer along with the unfocused light and is capable of obtaining centimeter scale depth information. A technical challenge for VPAT is the unavailability of a laser source having sufficient energy for diffused photon excitation of the entire object. The optical parametric oscillator currently used for PAT has been designed for excitation of hemoglobin and other contrast agents in wavelength below 950 nm. Specifically, using a Nd:YAG laser as the pump source, the wavelengths above 1064 nm are provided by the idler beam of the optical parametric oscillator at very low conversion efficiency.

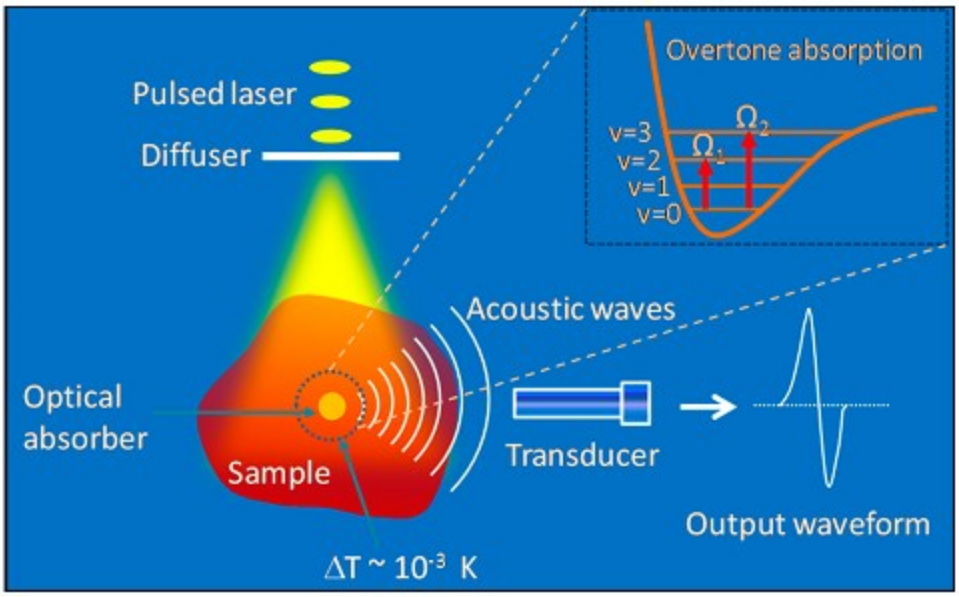

Figure 2-7: Signal generation and detection in VPAT. v = 0, 1, 2, and 3 denote ground and excited vibrational states.

Figure 2-7 shows the overtone vibrational absorption and photoacoustic wave generation processes. Vibrational absorption takes place when the incident photon frequency matches a transition frequency between the vibrational states (v). The (n-1)th overtone absorption takes place by transition from v = 0 to v = n, with n = 2, 3.... Unlike microscopy, in VPAT, the entire object is irradiated by the laser. Both the scattered and non-scattered photons contribute to the overtone absorption and subsequent generation of PA waves. Since the imaging depth is primarily determined by how deep the light can reach in a given sample, pulse energy of tens of mJ or more is required for an object of few cubic cm in size.

2.4.2 Theoretical Simulation

To evaluate the effect of scattering and absorption on VPAT imaging depth, we estimated the photon energy density in deep tissue at 1200 nm by Monte Carlo simulations[60] and compared it to that at 800 nm, where PAT imaging of blood is often performed. For the simulation, we considered a tissue with two layers, dermis of

thickness 0.4 cm and subcutaneous tissue of varying thickness from 0 to 2.6 cm. Tissue optical parameters such as absorption and scattering coefficients were obtained from reference[61] and a refractive index of 1.4 was assumed. The simulated energy density versus the depth is given in **Figure 2-8**. It is seen that at 3.0 cm depth, the light fluence is reduced by ~8 orders of magnitude, suggesting the need for high energy laser to perform VPAT. Moreover, it is noted that the fluence for 1200 nm at 2.0 cm depth is 5 times higher than that for 800 nm. Such enhancement is due to lower scattering coefficients at longer wavelengths. Since the PA signal is proportional to light fluence, this result indicates that 1200 nm excitation is beneficial for deep tissue vibrational imaging.

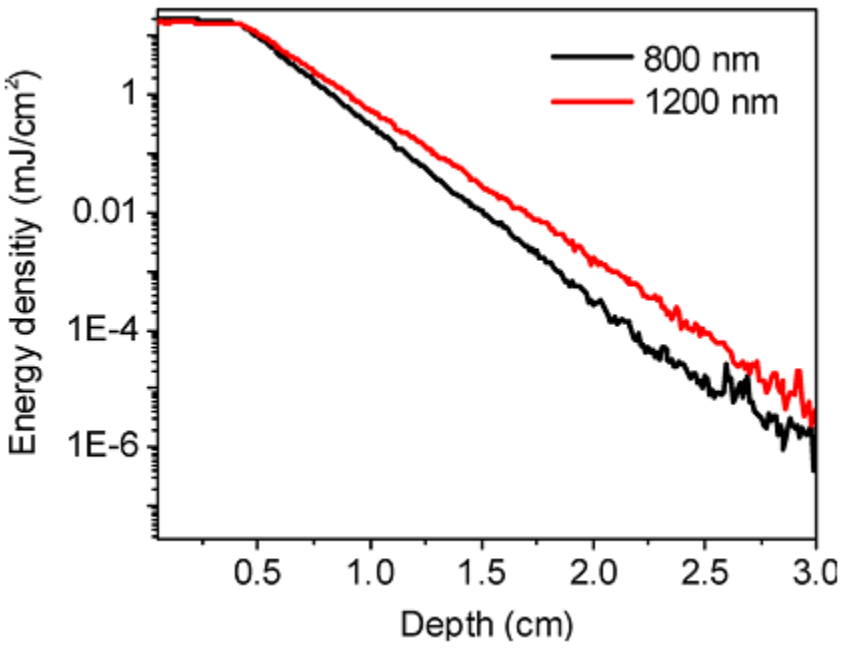

Figure 2-8: Energy density (fluence) versus depth by Monte Carlo simulation on a tissue with a dermis layer (μ_a=0.11cm^{-1}, μ_s'=2.18cm^{-1} at 800 nm & μ_a=0.13 cm^{-1}, μ_s'=1.65 cm^{-1} at 1200 nm) and a subcutaneous layer (μ_a=1.07 cm^{-1}, μ_s'=11.6 cm^{-1} at 800 nm & μ_a=1.06 cm^{-1}, μ_s'=7.91cm^{-1} at 1200 nm).

2.4.3 Experimental Setup and Performance of the Raman Laser

Schematic of our Raman laser is given in **Figure 2-9 (a)**. An 1064 nm Nd:YAG laser beam with 5 ns pulse width and 10 Hz repetition rate, after deflection by mirrors M_1 and M_2, passes through a polarizing beam splitter (PBS) to purify the polarization. Then it passes through a half wave plate and a second PBS. This combination is used to adjust the input pulse energy to obtain the desired output. After deflection by mirrors M_3 and M_4, the beam enters into the cavity through a quarter wave plate, which protects the Nd:YAG laser from perturbation by backscattered light. The laser cavity contains a $Ba(NO_3)_2$ crystal with size of $8\times8\times80$ mm^3 placed between mirrors M_5 and M_6. These mirrors were coated such that M_5 has high reflectivity at 1197 nm and high transmission at 1064 nm and M_6 has high reflectivity at 1064 nm and 40% transmission at 1197 nm.

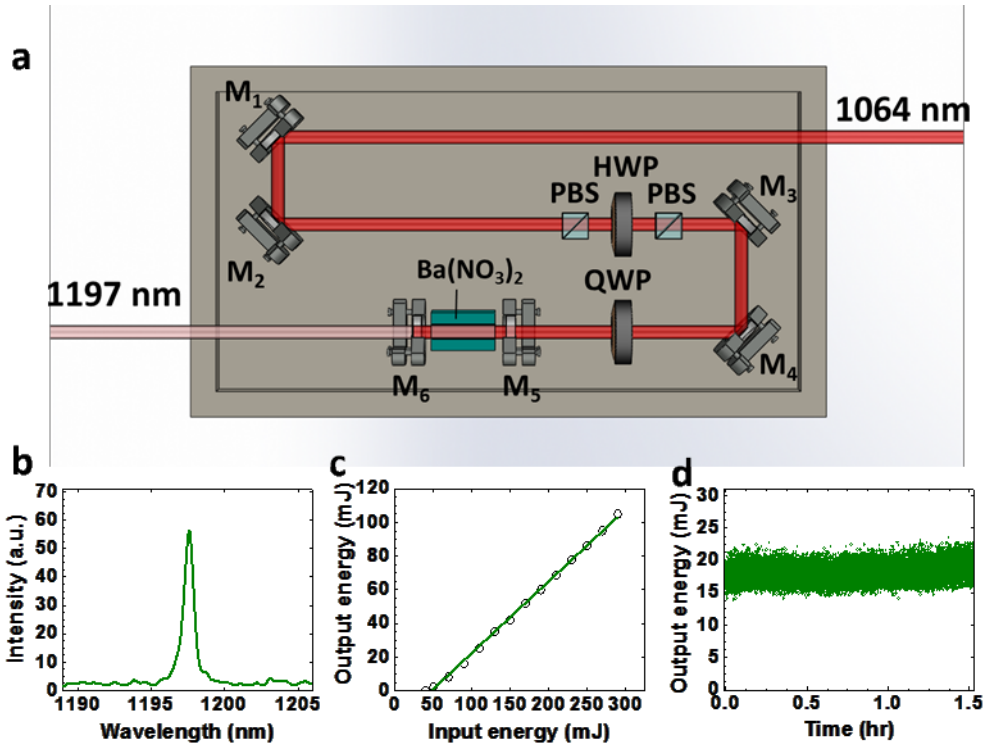

Figure 2-9: Setup and performance of the Raman laser. (a) Schematic; (b) Output spectral profile measured by a USB2000 spectrometer; (c) Output energy versus the input; (d) Output energy versus time. PBS: polarizing beam splitter. HWP: half wave plate. QWP: quarter wave plate.

The Raman laser outputs pulses with a narrow spectrum centered at 1197 nm as given in **Figure 2-9 (b)**. Performance of the laser was tested by measuring the output energy versus the input energy. Also, the energy was monitored as a function of time to examine the long term stability. The plot of the output versus the input energy is given in **Figure 2-9 (c)**. It is seen that, the output energy varies linearly with the input in the range from 50 to 290 mJ. With the input energy of 290 mJ, an output of 105 mJ was obtained at 1197 nm, corresponding to a conversion efficiency of 36%. Such efficiency is higher than current optical parametric oscillator technology by ~100 times at the specified wavelength. The Raman laser showed high stability over a time period of 1.5 hr as seen in **Figure 2-9 (d)**. This stability is important to acquire high quality tomography images.

2.4.4 Experimental Setup of VPAT with a Single Element Transducer

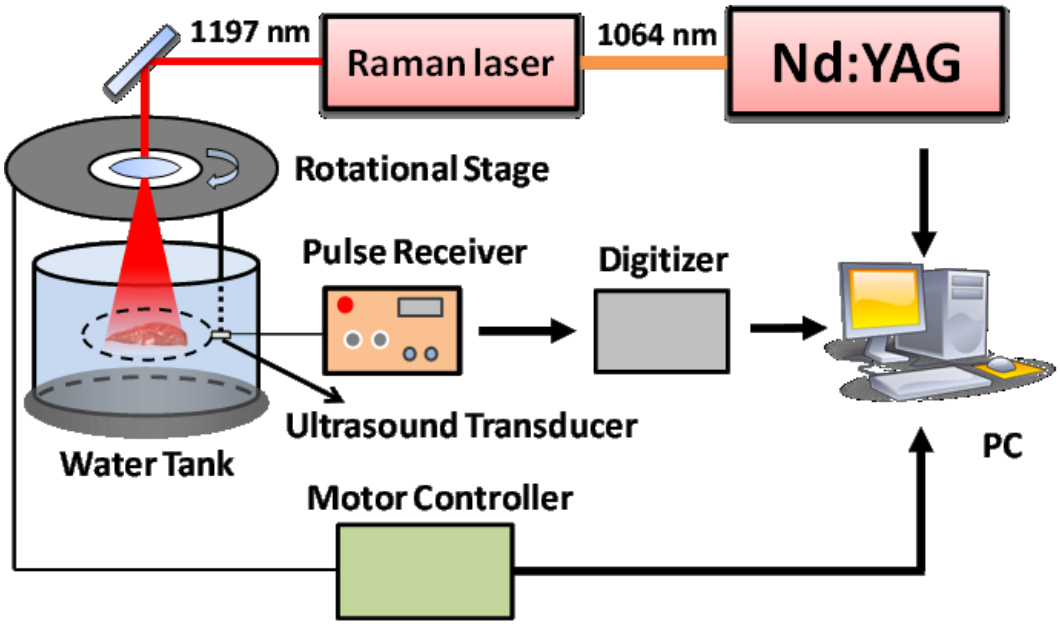

Figure 2-10: Schematic of VPAT system. A single transducer rotating around the object was used to collect the PA signal.

Schematic of our VPAT imaging system is given in **Figure 2-10**. The 1197 nm laser output from the Raman laser delivering high energy pulses at 10 Hz was used to irradiate the sample. These laser pulses pass through the center hole of a computer controlled rotational stage before reaching the sample. An unfocused 10-MHz, 2-mm diameter ultrasonic transducer (XMS 310, Olympus NDT) attached to the rotational stage was used to receive the PA signal. The transducer and the sample were placed inside a water tank to provide acoustic coupling between them. The transducer output was connected to a 20 dB preamplifier followed by a pulser/receiver (5072PR, Panametrics NDT) with gain of 20 dB. Then it was sent into a data acquisition (DAQ) card, which was triggered by the Q-switch of the Nd:YAG laser. During imaging, the rotational stage was moved in steps around the sample in a circular path of radius 4.5 cm and the PA signal was acquired for each step until one complete revolution. A LabVIEW program was used to control the rotational stage and collect the data.

2.4.5 Cell Viability Test

In our VPAT experiments, depending upon the sample size, laser fluence up to 100 mJ/cm^2 was used for irradiation. Although this energy is below the limit set by ANSI safety standards for the laser wavelength used, it is desirable to study whether the laser pulses pose any serious harm to the cells in the tissues.[62] Therefore, we performed a standard cell viability test using six well plates containing cultured human prostate cancer PC3 cells. Three of them were irradiated for 30 sec by 1197 nm laser pulses with 100 mJ/cm^2 energy density. Immediately after irradiation, cells were stained by calcein and propidium iodide for 15 min and then imaged on a confocal microscope. Number of damaged cells and viable cells were counted, based on the staining by propidium iodide and calcein, respectively. Typical micrographs of control and irradiated cells and the average cell viability for each group are given in **Figure 2-11**.

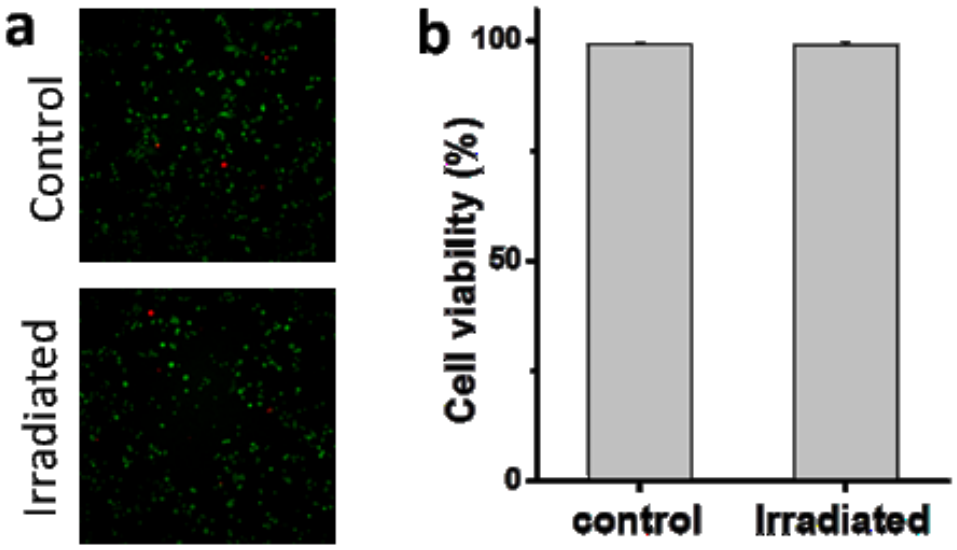

Figure 2-11: Results of cell viability test. (a) Confocal fluorescence microscopy images (Green: calcein, red: propidium iodide) of control prostate cells and the prostate cells irradiated with 100 mJ/cm^2 density laser pulses at 1197 nm. (b) Viability of control and irradiated cells. Cell viability was calculated by dividing the number of viable cells with the total number of cells in each well.

2.4.6 Result and Discussion

A phantom made of a polyethylene tube was used to demonstrate the proof-of-concept of VPAT. The tube has an outer diameter of 1.0 mm and an inner diameter of 0.6 mm. This material was selected because it is rich in C-H bonds, which is evident in the PA spectrum of polyethylene given in **Figure 2-12 (a)**. In the spectral window shown here, there are two bands, one peaked at ~ 1200 nm and the other peaked at ~ 1440 nm. The first band centered at 1200 nm corresponds to the second overtone absorption of C-H bond stretching vibration. The wavelength of the Raman laser used in this study is within this absorption band. To explore the imaging depth limit, we performed one-dimensional PA measurements on a 3 mm long polyethylene tube sample. Fresh chicken breast tissue layer was placed above the sample to mimic the in vivo situation. Laser energy of 57 mJ/cm^2 was sent to the sample through the chicken tissue layer. The layer

thickness was varied and the corresponding PA signal from the sample was measured. Then, the peak to peak amplitude of the PA signal was estimated. The plot of which is given in **Figure 2-12 (b)**. It shows a variation of more than three orders of magnitude in PA amplitude over 3 cm thickness range. The pattern of the plot follows a linear relationship in log scale which is reasonable based on the Beer's law. It should be noted that, even for a thickness of 3 cm, we could obtain signal from the target with a signal to noise ratio of 2.5 as shown **Figure 2-12 (c)**. To obtain this data at 3 cm depth, we performed an average of 100 pulse excitations and a group of 20 data sets were taken and then averaged. For other depths, due to higher signal to noise ratio, averages of smaller number of pulses were carried out. Since part of the light was absorbed by the chicken tissue, there was also PA signal emanated from it, as marked in **Figure 2-12 (c)**. The chicken tissue was placed at a distance from the polyethylene tube, so that we could easily separate the two PA signals based on the time delay.

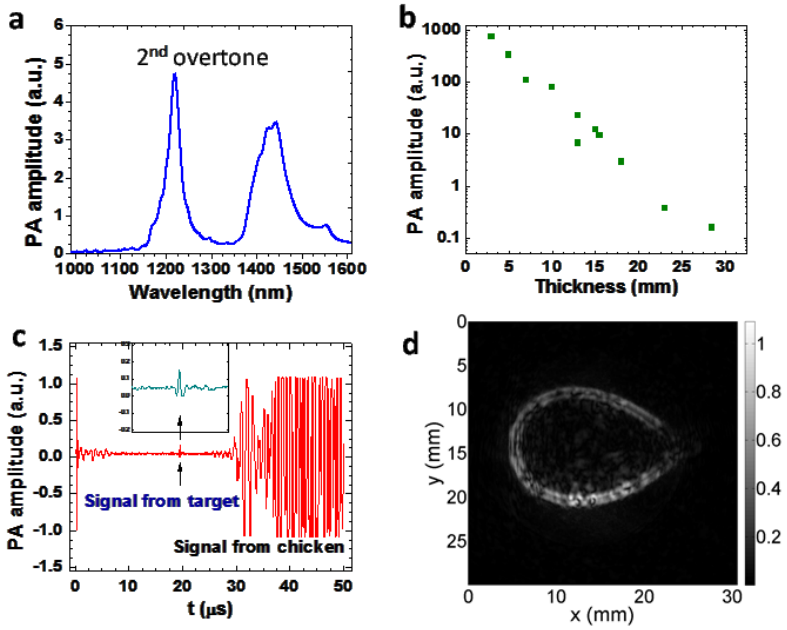

Figure 2-12: VPAT imaging of a polyethylene tube placed under a chicken breast tissue. (a) PA spectrum of polyethylene; (b) PA signal amplitude versus chicken layer thickness; (c) PA signal with 3 cm thick chicken breast layer; (d) VPAT image of a polyethylene tube ring placed under a 5 mm chicken breast tissue.

Two dimensional VPAT imaging was performed with a phantom made out of the same polyethylene tube. Two ends of a piece of the tube were joined together by using an epoxy to form a ring shape. The ring was then placed approximately at the center of the circular path of the transducer by gluing it on a glass tube with epoxy. A 5 mm thick chicken breast layer was placed at a distance of 5 mm above the ring. Pulses from the Raman laser set at 80 mJ with a beam diameter of 1.0 cm irradiated the chicken tissue and illuminated the ring. The transducer was rotated in steps of 2° and the PA signal was collected for each step at a rate of 100 kHz, until a complete revolution. Ten pulses were averaged for each measurement. It took about 10 minutes for acquisition of a complete set of data. The image was then reconstructed using a modified back projection algorithm.[63] An image of the polyethylene ring obtained from the VPAT system is given in **Figure 2-12(d)**. The image showed a good contrast with undetectable background contributed by water at the wavelength of 1197 nm.

2.4.7 Conclusion

In summary, we have demonstrated a vibrational photoacoustic tomography imaging system enabled by a high energy Raman laser at 1197 nm. Using this system, we have obtained vibrational photoacoustic signal from C-H rich polyethylene tube placed below 3 cm chicken breast tissue with input laser pulse energy well below the ANSI safety limit. VPAT image of polyethylene tube placed under 5 mm chicken tissue was achieved with excellent contrast. We note that the single element system in this study is slow in data acquisition as compared to linear array transducer being used for PAT or ultrasound imaging. Future work will focus on using linear arrays and commercially available ultrasound machine for in vivo imaging.

2.5 Vibrational Photoacoustic Tomography with Transducer Array

Proof-of-concept of vibrational photoacoustic tomography has been demonstrated with a homebuilt Raman laser generating greater than 100 mJ of energy per pulse at 1197 nm wavelength. In our preliminary studies, a single element transducer was used to record generated photoacoustic signal. Although its signal quality is good, the slow imaging speed caused by transducer scanning restricts its applications from bench to bedside.

2.5.1 VPAT in Free Space

Figure 2-13: Vevo 2100 system. FUJIFILM VisualSonics Inc.

In collaboration with Dr. Craig Goergen at Weldon School of Biomedical Engineering at Purdue University, we built a vibrational photoacoustic tomography imaging system based on Vevo 2100 ultrasound machine. The Vevo 2100 system

(FUJIFILM VisualSonics Inc.) is a high-frequency, high-resolution imaging platform with linear array technology. (**Figure 2-13**) The schematic of our VPAT imaging system is shown in **Figure 2-14**. The 1197 nm Raman laser pumped by the fundamental light of Nd:YAG laser directly illuminates the sample, which is immersed in a water tank filled with tapping water. The MS 550 transducer with 40 MHz central frequency is located exactly above the sample. In order to avoid impedance mismatch, the transmitting end of the transducer is also immersed into water. Since polyethylene ring is rich of CH-bond, it is used as the phantom to generate PA signal at 1197 nm. The image is shown in **Figure 2-15**. The left one is ultrasound image, while the right one is photoacoustic image. In the experiment, 70 mJ pulse energy at 1197 nm is applied to illuminate the ring, while the imaging depth could reach to 1.2 cm. Here, the imaging depth is not limited by light attenuation in the water, but by the small illumination area of the light.

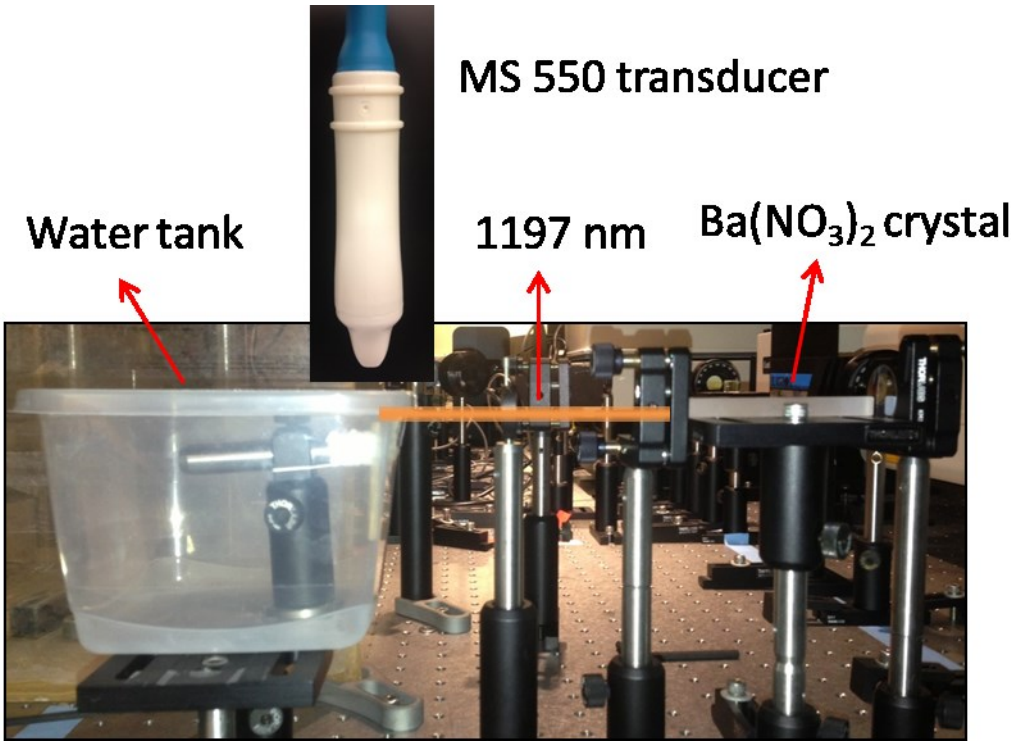

Figure 2-14: Setup of VPAT system in free space with a high pulse energy Raman laser based on $Ba(NO_3)_2$ crystal

Figure 2-15: VPAT images of polyethylene tube.

2.5.2 VPAT with Optical Fiber Bundle

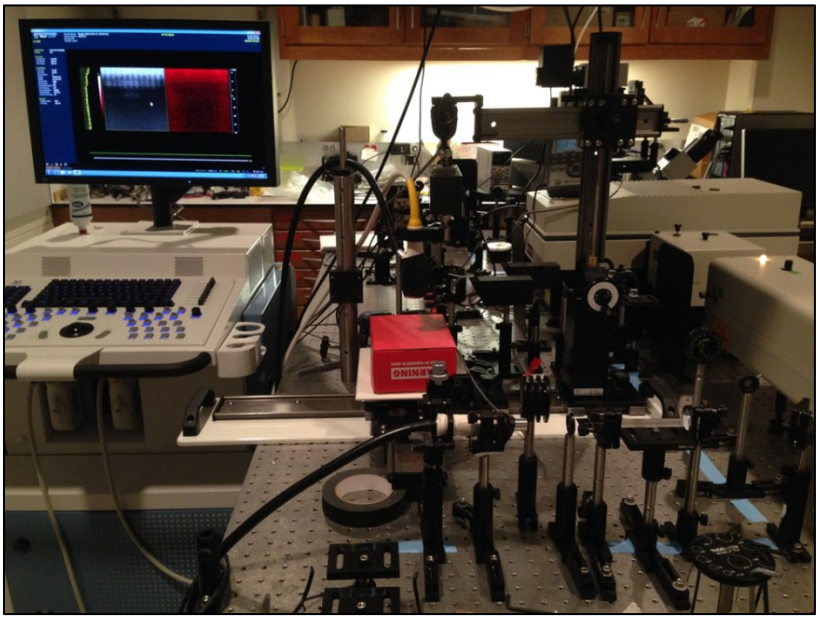

Figure 2-16: Schematic of VPAT system with integrated fiber bundle and transducer array.

Although VPAT imaging system in free space could get good signal, it is not convenient for use in hospital. In order to make it more compact and flexible, an optical fiber bundle with 60 % transmission at 1197 nm is integrated with the ultrasound transducer. In our preliminary studies, the fiber bundle is stabilized with the transducer using by electric tape. The whole VPAT system is shown in **Figure 2-16**. The transducer is stabilized by a stage, which can be used for 3D scanning. Based on this platform, we performed PA imaging of normal liver and fatty liver harvested from mice (**Figure 2-17**). The samples are put in ultrasonic gel for acoustic match. The central frequency of transducer (MS 250) is 16 MHz, and the pulse energy of the laser is 60 mJ. From ultrasound image (**Figure 2-17 (a)**), we could see both of them clearly. However, in PA image averaged 100 times (**Figure 2-17 (b)**), we could only see fatty liver which is rich of CH-bond.

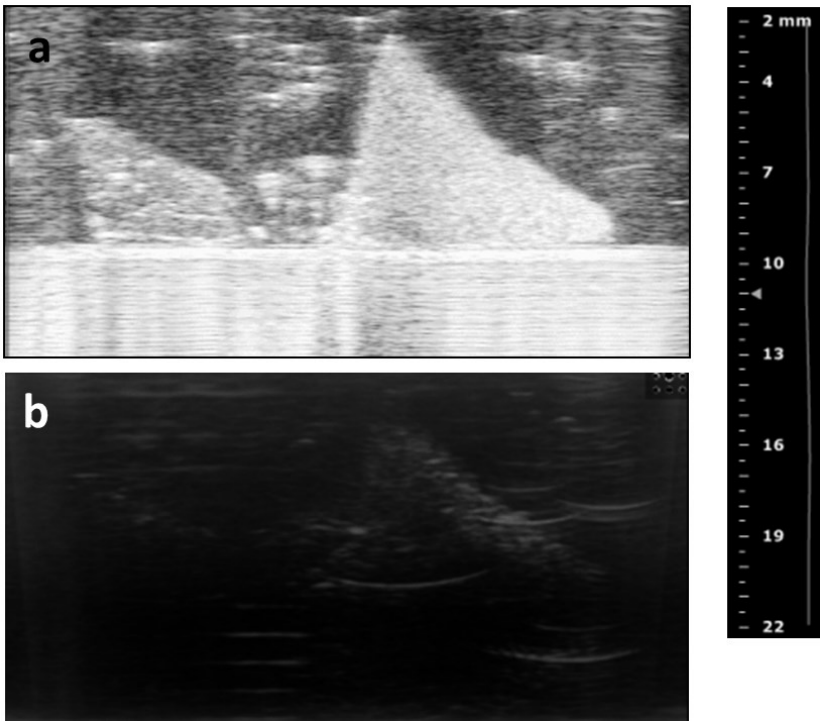

Figure 2-17: Ultrasound and photoacoustic images of liver samples from mice. (a) Ultrasound image of mice liver. (b) Photoacoustic images of mice liver.

CHAPTER 3. FUTURE WORK AND CONCLUSIONS

3.1 Future Work

Abdominal aortic aneurysm (AAA) is a complex disease defined as the pathologic dilation of the vessel wall. Clinically, an aortic diameter 150% larger than normal is considered diseased,[64] although most AAAs are asymptomatic and only surgical treatment options currently exist. Anywhere between 5% and 10% of people in the industrialized world over the age of 65 suffer from AAAs,[65-66] accounting for roughly 16,000 deaths and 150,000 inpatient hospitalizations per year in the United States.[67-68] Although basic science and clinical studies have led insight into the problems associated with AAAs, a detailed understanding of the underlying mechanisms that lead to AAA development and expansion still remains incomplete. Mouse models of AAAs instigated by genetic and chemical induction have provided insight into potential mechanisms for the development of the disease. Systemic infusion of angiotensin II (AngII) into apolipoprotein $E^{-/-}$ ($apoE^{-/-}$) mice has been shown to lead to atherosclerosis and suprarenal abdominal aortic aneurysms.[69] In the aorta, there is a mixture composed of lipid, collagen, and elastin. Understanding the underlying makeup of the aortic wall will play an important role in aneurysm expansion.

Vibrational photoacoustic imaging has shown the capability to map lipid distribution in the biological samples using a single wavelength.[70] Furthermore, lipid and collagen can be distinguished by multispectral photoacoustic imaging of the first

overtone of CH-bond,[71] which provide us an opportunity to image the composition of AAA disease.

To fulfill this aim, firstly, based on our existing VPAT platform, we will perform photoacoustic and ultrasound imaging to map lipid distribution in AAA using apoE$^{-/-}$ mice model *in vivo*. Then, we will build a chemically-selective multispectral dual-modality photoacoustic and ultrasound imaging system capable of quantifying signal from fat, collagen in small animals. A customized high-energy Nd:YAG pumped optical parametric oscillator will be used as the irradiation source, in combination with Vevo 2100 system to acquire photoacoustic signal over a range of excitation wavelengths. To ensure statistical significance, 40 apoE$^{-/-}$ mice (B6.129P2-Apoe^{tm1Unc}/J, Jackson Laboratories, Bar Harbor, ME) will be implanted with AngII (A9525, Sigma-Aldrich, St. Louis, MO) filled osmotic pumps (model 2004, Durect Corporation, Cupertino, CA).[69] These pumps release AngII at a rate of 1000 ng/kg/min over 28 days. We will also infuse pancreatic porcine elastase (E1250, Sigma-Aldrich) at a pressure of 100 mmHg into the infrarenal aortas of 40 Sprague Dawley rats (Harlan Laboratories, Indianapolis, IN). Twenty additional apoE$^{-/-}$ mice will be implanted with saline filled pumps and used as healthy controls. Similarly, a control group of twenty Sprague Dawley rats will be infused with heat-inactivated elastase. Imaging with the photoacoustic system will be done before AAA induction and on days 3, 7, 14, 21, and 28. Photoacoustic images will be acquired that can noninvasively characterize aortic wall composition in multiple experimental AAA models. In addition, we expect our histological analysis to confirm the composition of the arterial wall.

What's more, VPAT imaging of human atherosclerotic arteries will be performed to characterize its chemical composition. Firstly, agrose gel-based phantom will be made to mimic the tissue scattering properties.[72-73] Then, human atherosclerotic arteries will be immersed into the gel for photoacoustic imaging *in vitro*.

3.2 Conclusion

With optical absorption contrast and ultrasonic spatial resolution, photoacoustic (PA) tomography has been applied to animals or human organs such as breast, brain and skin. In the past, the majority of the PA imaging studies has been based on electronic absorption of molecules and nanostructures. Photoacoustic imaging employing molecular overtone vibration as a contrast mechanism opens a new avenue for bond-selective imaging of deep tissues. In particular, overtones of C-H bond vibration have been adopted to visualize lipid and collagen. In order to resonate with C-H bond vibration, laser wavelengths at 1210 nm or 1730 nm are used, where the absorption peaks of the second and first overtone reside. Currently, the optical parametric oscillator (OPO) pumped by harmonics of Nd:YAG laser is employed to generate the necessary wavelengths. However, the conversion efficiency at the aforementioned specific wavelengths is very low, making it difficult to generate high pulse energy needed for vibrational PA tomography. In addition, the cost of an OPO often exceeds that of the pump laser.

To overcome such a barrier, we describe an approach to address the aforementioned barriers by efficiently shifting the wavelength of a Nd:YAG laser with a homebuilt solid-state Raman laser. Using a 5-ns Nd:YAG laser as the pumping source, up to 21.4 mJ pulse energy at 1197 nm was generated, corresponding to a conversion efficiency of 34.8%. Using the 1197 nm pulses, three-dimensional photoacoustic imaging of intramuscular fat was demonstrated to verify the feasibility and capability of the Raman laser.

By using a larger $Ba(NO_3)_2$ crystal and no prior focusing of input laser, our new Raman laser is able to produce stable laser pulses at 1197 nm with maximum pulse energy exceeding 100 mJ. Based on the new laser system, vibrational photoacoustic tomography signal from C-H rich polyethylene tube phantom placed under 3 cm thick chicken breast tissue was obtained with a signal to noise ratio of 2.5. Further, we

recorded photoacoustic image of a polyethylene ring placed under 5 mm chicken tissue with excellent contrast. Although its signal quality is good, the slow imaging speed caused by transducer scanning restricts its applications from bench to bedside.

At last, in collaboration with Dr. Craig Goergen at Purdue University, we built a vibrational photoacoustic tomography imaging system based on Vevo 2100 ultrasound machine, which could fulfill photoacoustic and ultrasound imaging in real time. VPAT imaging of polyethylene ring is performed in free space to demonstrate its feasibility. By integrating with a fiber bundle, a more convenient and compact VPAT platform is built. Normal liver and fatty liver of mice are used to demonstrate its capability to image lipid composition in biological samples.

LITERATURE CITED

LITERATURE CITED

1. Bell, A. G. The Photophone. *Science* **1880,** *1* (11), 130-4.

2. Bell, A. G. The Production of Sound by Radiant Energy. *Science* **1881,** *2* (49), 242-53.

3. Rosencwaig, A. Photoacoustic Spectroscopy. *Annual review of biophysics and bioengineering* **1980,** *9*, 31-54.

4. Small, J. R. Deconvolution Analysis for Pulsed-Laser Photoacoustics. *Methods in enzymology* **1992,** *210*, 505-21.

5. Cheng, J. X. Coherent Anti-Stokes Raman Scattering Microscopy. *Applied spectroscopy* **2007,** *61* (9), 197-208.

6. Han, M.; Giese, G.; Bille, J. Second Harmonic Generation Imaging of Collagen Fibrils in Cornea and Sclera. *Optics express* **2005,** *13* (15), 5791-7.

7. Rajadhyaksha, M.; Grossman, M.; Esterowitz, D.; Webb, R. H.; Anderson, R. R. In Vivo Confocal Scanning Laser Microscopy of Human Skin: Melanin Provides Strong Contrast. *The Journal of investigative dermatology* **1995,** *104* (6), 946-52.

8. Keller, T. S.; Mao, Z.; Spengler, D. M. Young's Modulus, Bending Strength, and Tissue Physical Properties of Human Compact Bone. *Journal of orthopaedic research : official publication of the Orthopaedic Research Society* **1990,** *8* (4), 592-603.

9. Folkman, J. Tumor Angiogenesis in Women with Node-Positive Breast Cancer. *The cancer journal from Scientific American* **1995,** *1* (2), 106-8.

10. Weidner, N.; Semple, J. P.; Welch, W. R.; Folkman, J. Tumor Angiogenesis and Metastasis--Correlation in Invasive Breast Carcinoma. *The New England journal of medicine* **1991,** *324* (1), 1-8.

11. Huang, D.; Swanson, E. A.; Lin, C. P.; Schuman, J. S.; Stinson, W. G.; Chang, W.; Hee, M. R.; Flotte, T.; Gregory, K.; Puliafito, C. A.; et al. Optical Coherence Tomography. *Science* **1991,** *254* (5035), 1178-81.

12. Frangioni, J. V. In Vivo near-Infrared Fluorescence Imaging. *Current opinion in chemical biology* **2003,** *7* (5), 626-34.

13. Hawrysz, D. J.; Sevick-Muraca, E. M. Developments toward Diagnostic Breast Cancer Imaging Using near-Infrared Optical Measurements and Fluorescent Contrast Agents. *Neoplasia* **2000,** *2* (5), 388-417.

14. Tromberg, B. J.; Shah, N.; Lanning, R.; Cerussi, A.; Espinoza, J.; Pham, T.; Svaasand, L.; Butler, J. Non-Invasive in Vivo Characterization of Breast Tumors Using Photon Migration Spectroscopy. *Neoplasia* **2000,** *2* (1-2), 26-40.

15. Jacques, S. L. Optical Properties of Biological Tissues: A Review. *Physics in medicine and biology* **2013,** *58* (11), R37-61.

16. Ku, G.; Fornage, B. D.; Jin, X.; Xu, M.; Hunt, K. K.; Wang, L. V. Thermoacoustic and Photoacoustic Tomography of Thick Biological Tissues toward Breast Imaging. *Technology in cancer research & treatment* **2005,** *4* (5), 559-66.

17. Ku, G.; Wang, X.; Stoica, G.; Wang, L. V. Multiple-Bandwidth Photoacoustic Tomography. *Physics in medicine and biology* **2004,** *49* (7), 1329-38.

18. Wang, X.; Pang, Y.; Ku, G.; Xie, X.; Stoica, G.; Wang, L. V. Noninvasive Laser-Induced Photoacoustic Tomography for Structural and Functional in Vivo Imaging of the Brain. *Nature biotechnology* **2003,** *21* (7), 803-6.

19. Wang, X.; Xie, X.; Ku, G.; Wang, L. V.; Stoica, G. Noninvasive Imaging of Hemoglobin Concentration and Oxygenation in the Rat Brain Using High-Resolution Photoacoustic Tomography. *Journal of biomedical optics* **2006,** *11* (2), 024015.

20. Zhang, H. F.; Maslov, K.; Stoica, G.; Wang, L. V. Functional Photoacoustic Microscopy for High-Resolution and Noninvasive in Vivo Imaging. *Nature biotechnology* **2006,** *24* (7), 848-51.

21. Brecht, H. P.; Su, R.; Fronheiser, M.; Ermilov, S. A.; Conjusteau, A.; Oraevsky, A. A. Whole-Body Three-Dimensional Optoacoustic Tomography System for Small Animals. *Journal of biomedical optics* **2009,** *14* (6), 064007.

22. Laufer, J.; Delpy, D.; Elwell, C.; Beard, P. Quantitative Spatially Resolved Measurement of Tissue Chromophore Concentrations Using Photoacoustic Spectroscopy: Application to the Measurement of Blood Oxygenation and Haemoglobin Concentration. *Physics in medicine and biology* **2007,** *52* (1), 141-68.

23. Rajian, J. R.; Girish, G.; Wang, X. Photoacoustic Tomography to Identify Inflammatory Arthritis. *Journal of biomedical optics* **2012,** *17* (9), 96013-1.

24. Akers, W. J.; Kim, C.; Berezin, M.; Guo, K.; Fuhrhop, R.; Lanza, G. M.; Fischer, G. M.; Daltrozzo, E.; Zumbusch, A.; Cai, X.; Wang, L. V.; Achilefu, S. Noninvasive Photoacoustic and Fluorescence Sentinel Lymph Node Identification Using Dye-Loaded Perfluorocarbon Nanoparticles. *ACS nano* **2011,** *5* (1), 173-82.

25. Kim, J. W.; Galanzha, E. I.; Shashkov, E. V.; Moon, H. M.; Zharov, V. P. Golden Carbon Nanotubes as Multimodal Photoacoustic and Photothermal High-Contrast Molecular Agents. *Nature nanotechnology* **2009,** *4* (10), 688-94.

26. Taruttis, A.; Herzog, E.; Razansky, D.; Ntziachristos, V. Real-Time Imaging of Cardiovascular Dynamics and Circulating Gold Nanorods with Multispectral Optoacoustic Tomography. *Optics express* **2010,** *18* (19), 19592-602.

27. Zhang, Q.; Iwakuma, N.; Sharma, P.; Moudgil, B. M.; Wu, C.; McNeill, J.; Jiang, H.; Grobmyer, S. R. Gold Nanoparticles as a Contrast Agent for in Vivo Tumor Imaging with Photoacoustic Tomography. *Nanotechnology* **2009,** *20* (39), 395102.

28. Wang, L. V.; Hu, S. Photoacoustic Tomography: In Vivo Imaging from Organelles to Organs. *Science* **2012,** *335* (6075), 1458-62.

29. Hu, S.; Maslov, K.; Wang, L. V. Second-Generation Optical-Resolution Photoacoustic Microscopy with Improved Sensitivity and Speed. *Optics letters* **2011,** *36* (7), 1134-6.

30. Jansen, K.; van der Steen, A. F.; van Beusekom, H. M.; Oosterhuis, J. W.; van Soest, G. Intravascular Photoacoustic Imaging of Human Coronary Atherosclerosis. *Optics letters* **2011,** *36* (5), 597-9.

31. Wang, B.; Yantsen, E.; Larson, T.; Karpiouk, A. B.; Sethuraman, S.; Su, J. L.; Sokolov, K.; Emelianov, S. Y. Plasmonic Intravascular Photoacoustic Imaging for Detection of Macrophages in Atherosclerotic Plaques. *Nano letters* **2009,** *9* (6), 2212-7.

32. Yang, J. M.; Maslov, K.; Yang, H. C.; Zhou, Q.; Shung, K. K.; Wang, L. V. Photoacoustic Endoscopy. *Optics letters* **2009,** *34* (10), 1591-3.

33. Yang, Y.; Li, X.; Wang, T.; Kumavor, P. D.; Aguirre, A.; Shung, K. K.; Zhou, Q.; Sanders, M.; Brewer, M.; Zhu, Q. Integrated Optical Coherence Tomography, Ultrasound and Photoacoustic Imaging for Ovarian Tissue Characterization. *Biomedical optics express* **2011,** *2* (9), 2551-61.

34. Gamelin, J.; Aguirre, A.; Maurudis, A.; Huang, F.; Castillo, D.; Wang, L. V.; Zhu, Q. Curved Array Photoacoustic Tomographic System for Small Animal Imaging. *Journal of biomedical optics* **2008,** *13* (2), 024007.

35. Kim, C.; Favazza, C.; Wang, L. V. In Vivo Photoacoustic Tomography of Chemicals: High-Resolution Functional and Molecular Optical Imaging at New Depths. *Chemical reviews* **2010,** *110* (5), 2756-82.

36. Kruger, R. A.; Lam, R. B.; Reinecke, D. R.; Del Rio, S. P.; Doyle, R. P. Photoacoustic Angiography of the Breast. *Medical physics* **2010,** *37* (11), 6096-100.

37. Manohar, S.; Kharine, A.; van Hespen, J. C.; Steenbergen, W.; van Leeuwen, T. G. Photoacoustic Mammography Laboratory Prototype: Imaging of Breast Tissue Phantoms. *Journal of biomedical optics* **2004,** *9* (6), 1172-81.

38. Allen, T. J.; Hall, A.; Dhillon, A. P.; Owen, J. S.; Beard, P. C. Spectroscopic Photoacoustic Imaging of Lipid-Rich Plaques in the Human Aorta in the 740 to 1400 Nm Wavelength Range. *Journal of biomedical optics* **2012,** *17* (6), 061209.

39. Wang, H. W.; Chai, N.; Wang, P.; Hu, S.; Dou, W.; Umulis, D.; Wang, L. V.; Sturek, M.; Lucht, R.; Cheng, J. X. Label-Free Bond-Selective Imaging by Listening to Vibrationally Excited Molecules. *Physical review letters* **2011,** *106* (23), 238106.

40. Wang, P.; Wang, H. W.; Sturek, M.; Cheng, J. X. Bond-Selective Imaging of Deep Tissue through the Optical Window between 1600 and 1850 Nm. *Journal of biophotonics* **2012,** *5* (1), 25-32.

41. Wang, B.; Karpiouk, A.; Yeager, D.; Amirian, J.; Litovsky, S.; Smalling, R.; Emelianov, S. Intravascular Photoacoustic Imaging of Lipid in Atherosclerotic Plaques in the Presence of Luminal Blood. *Optics letters* **2012,** *37* (7), 1244-6.

42. Wang, B.; Su, J. L.; Amirian, J.; Litovsky, S. H.; Smalling, R.; Emelianov, S. Detection of Lipid in Atherosclerotic Vessels Using Ultrasound-Guided Spectroscopic Intravascular Photoacoustic Imaging. *Optics express* **2010,** *18* (5), 4889-97.

43. Anderson, R. R.; Farinelli, W.; Laubach, H.; Manstein, D.; Yaroslavsky, A. N.; Gubeli, J., 3rd; Jordan, K.; Neil, G. R.; Shinn, M.; Chandler, W.; Williams, G. P.; Benson, S. V.; Douglas, D. R.; Dylla, H. F. Selective Photothermolysis of Lipid-Rich Tissues: A Free Electron Laser Study. *Lasers in surgery and medicine* **2006,** *38* (10), 913-9.

44. Roos, P. A.; Brasseur, J. K.; Carlsten, J. L. Diode-Pumped Nonresonant Continuous-Wave Raman Laser in H2 with Resonant Optical Feedback Stabilization. *Optics letters* **1999,** *24* (16), 1130-2.

45. Roos, P. A.; Meng, L. S.; Carlsten, J. L. Doppler-Induced Unidirectional Operation of a Continuous-Wave Raman Ring Laser in H2. *Applied optics* **2003,** *42* (27), 5517-21.

46. Trutna, W. R.; Byer, R. L. Multiple-Pass Raman Gain Cell. *Applied optics* **1980,** *19* (2), 301-12.

47. Ding, M.; Koizumi, H.; Suzuki, Y. [High Performance Liquid Chromatographic Determination of Reducing Sugars in Fruit Juices with Laser Resonance Raman Detection]. *Se pu = Chinese journal of chromatography / Zhongguo hua xue hui* **1997,** *15* (4), 281-3.

48. Fang, W.; Li, Z.; Li, D.; Zhou, M.; Men, Z.; Sun, C. Stimulated Raman Scattering from Sulfur-Ii Produced by Laser Decomposition of Liquid Carbon Disulfide. *Optics letters* **2013,** *38* (6), 950-2.

49. Melveger, A. J.; Brasch, J. W.; Lippincott, E. R. Laser Raman Spectra of Liquid and Solid Bromine and Carbon Disulfide under High Pressure. *Applied optics* **1970,** *9* (1), 11-5.

50. Chen, Y. F. Compact Efficient All-Solid-State Eye-Safe Laser with Self-Frequency Raman Conversion in a Nd:Yvo4 Crystal. *Optics letters* **2004,** *29* (18), 2172-4.

51. Mildren, R.; Convery, M.; Pask, H.; Piper, J.; McKay, T. Efficient, All-Solid-State, Raman Laser in the Yellow, Orange and Red. *Optics express* **2004,** *12* (5), 785-90.

52. Mildren, R. P.; Coutts, D. W.; Spence, D. J. All-Solid-State Parametric Raman Anti-Stokes Laser at 508 Nm. *Optics express* **2009,** *17* (2), 810-8.

53. Mildren, R. P.; Ogilvy, H.; Piper, J. A. Solid-State Raman Laser Generating Discretely Tunable Ultraviolet between 266 and 320 Nm. *Optics letters* **2007,** *32* (7), 814-6.

54. Pask, H. M. Continuous-Wave, All-Solid-State, Intracavity Raman Laser. *Optics letters* **2005,** *30* (18), 2454-6.

55. Pask, H. M.; Myers, S.; Piper, J. A.; Richards, J.; McKay, T. High Average Power, All-Solid-State External Resonator Raman Laser. *Optics letters* **2003,** *28* (6), 435-7.

56. Cerny, P.; Jelinkova, H.; Zverev, P. G.; Basiev, T. T. Solid State Lasers with Raman Frequency Conversion. *Prog Quant Electron* **2004,** *28* (2), 113-143.

57. Pask, H. M. The Design and Operation of Solid-State Raman Lasers. *Prog Quant Electron* **2003,** *27* (1), 3-56.

58. Zverev, P. G.; Jia, W.; Liu, H.; Basiev, T. T. Vibrational Dynamic of the Raman-Active Mode in Barium Nitrate Crystal. *Optics letters* **1995,** *20* (23), 2378.

59. Wang, P.; Rajian, J. R.; Cheng, J. X. Spectroscopic Imaging of Deep Tissue through Photoacoustic Detection of Molecular Vibration. *The journal of physical chemistry letters* **2013,** *4* (13), 2177-2185.

60. Wang, L.; Jacques, S. L.; Zheng, L. Mcml--Monte Carlo Modeling of Light Transport in Multi-Layered Tissues. *Computer methods and programs in biomedicine* **1995,** *47* (2), 131-46.

61. Tuchin, V. *Tissue Optics: Light Scattering Methods and Instruments for Medical Diagnosis*. SPIE Press, Bellingham, Washington, USA: 2007.

62. America, L. I. o. American National Standard for Safe Use of Lasers Ansi Z136.1—2007. American National Standards Institute Orlando, FL, 2007.

63. Wang, X. D.; Xu, Y.; Xu, M. H.; Yokoo, S.; Fry, E. S.; Wang, L. H. V. Photoacoustic Tomography of Biological Tissues with High Cross-Section Resolution: Reconstruction and Experiment. *Medical physics* **2002,** *29* (12), 2799-2805.

64. Goergen, C. J.; Johnson, B. L.; Greve, J. M.; Taylor, C. A.; Zarins, C. K. Increased Anterior Abdominal Aortic Wall Motion: Possible Role in Aneurysm Pathogenesis and Design of Endovascular Devices. *J Endovasc Ther* **2007,** *14* (4), 574-84.

65. Scott, R. A.; Bridgewater, S. G.; Ashton, H. A. Randomized Clinical Trial of Screening for Abdominal Aortic Aneurysm in Women. *Br J Surg* **2002,** *89* (3), 283-5.

66. Silverstein, M. D.; Pitts, S. R.; Chaikof, E. L.; Ballard, D. J. Abdominal Aortic Aneurysm (Aaa): Cost-Effectiveness of Screening, Surveillance of Intermediate-Sized Aaa, and Management of Symptomatic Aaa. *Proc (Bayl Univ Med Cent)* **2005,** *18* (4), 345-67.

67. Ailawadi, G.; Eliason, J. L.; Upchurch, G. R., Jr. Current Concepts in the Pathogenesis of Abdominal Aortic Aneurysm. *J Vasc Surg* **2003,** *38* (3), 584-8.

68. Fleming, C.; Whitlock, E. P.; Beil, T. L.; Lederle, F. A. Screening for Abdominal Aortic Aneurysm: A Best-Evidence Systematic Review for the U.S. Preventive Services Task Force. *Ann Intern Med* **2005,** *142* (3), 203-11.

69. Daugherty, A.; Manning, M. W.; Cassis, L. A. Angiotensin Ii Promotes Atherosclerotic Lesions and Aneurysms in Apolipoprotein E-Deficient Mice. *J Clin Invest* **2000,** *105* (11), 1605-12.

70. Li, R.; Slipchenko, M. N.; Wang, P.; Cheng, J. X. Compact High Power Barium Nitrite Crystal-Based Raman Laser at 1197 Nm for Photoacoustic Imaging of Fat. *Journal of biomedical optics* **2013,** *18* (4), 040502.

71. Wang, P.; Wang, H. W.; Cheng, J. X. Mapping Lipid and Collagen by Multispectral Photoacoustic Imaging of Chemical Bond Vibration. *Journal of biomedical optics* **2012,** *17* (9), 96010-1.

72. Cook, J. R.; Bouchard, R. R.; Emelianov, S. Y. Tissue-Mimicking Phantoms for Photoacoustic and Ultrasonic Imaging. *Biomedical optics express* **2011,** *2* (11), 3193-206.

73. Kolkman, R. G.; Blomme, E.; Cool, T.; Bilcke, M.; van Leeuwen, T. G.; Steenbergen, W.; Grimbergen, K. A.; den Heeten, G. J. Feasibility of Noncontact Piezoelectric Detection of Photoacoustic Signals in Tissue-Mimicking Phantoms. *Journal of biomedical optics* **2010,** *15* (5), 055011.

PUBLICATIONS

PUBLICATIONS

Rui Li, Mikhail Slipchenko, Pu Wang, and Ji-Xin Cheng, “Compact high power barium nitrite crystal-based Raman laser at 1197 nm for photoacoustic imaging of fat,” J Biomed Opt, 2013. 18(4): p. 40502.

Justin Rajesh Rajian, Rui Li, Pu Wang, and Ji-Xin Cheng, “Vibrational photoacoustic tomography: chemical imaging beyond the ballistic regime,” J. Phys. Chem. Lett, 2013. 4: p. 3211-3215.

Aneesh Ramaswamy, Mark Hamilton II, Rucha Joshi, Benjamin Kline, Rui Li, Pu Wang and Craig Goergen, “Molecular imaging of experimental abdominal aortic aneurysms,” The Scientific World Journal, vol. 2013, Article ID 973150.

Rui Li, Justin Rajesh Rajian, Pu Wang, Mikhail N. Slipchenko, and Ji-Xin Cheng, “Vibration-based photoacoustic tomography,” BiOS Photonics West, SPIE, USA, 2013.